

European Extremely Large Telescope Site Characterization II: High angular resolution parameters

Héctor Vázquez Ramió

Instituto de Astrofísica de Canarias, c/ Vía Láctea s/n, E-38205, La Laguna, Tenerife, Spain
Departamento de Astrofísica; Universidad de La Laguna E-38205, La Laguna, Tenerife, Spain

`hvr@iac.es`

Jean Vernin

Université de Nice-Sophia Antipolis, Observatoire de la Côte d’Azur, CNRS-UMR7293,
Lagrange 06108 Nice Cedex 2, France

`vernin@unice.fr`

Casiana Muñoz-Tuñón

Instituto de Astrofísica de Canarias, c/ Vía Láctea s/n, E-38205, La Laguna, Tenerife, Spain
Departamento de Astrofísica; Universidad de La Laguna E-38205, La Laguna, Tenerife, Spain

`cmt@iac.es`

Marc Sarazin

European Southern Observatory, Karl-Schwarzschild-Str. 2 - 85748 Garching bei München.
Germany

`msarazin@eso.org`

Antonia M. Varela

Instituto de Astrofísica de Canarias, c/ Vía Láctea s/n, E-38205, La Laguna, Tenerife, Spain
Departamento de Astrofísica; Universidad de La Laguna E-38205, La Laguna, Tenerife, Spain

`avp@iac.es`

Hervé Trinquet

DGA Matrise de l’information, BP 7 35998 RENNES ARMEES, France

`herve.trinquet@dga.defense.gouv.fr`

José Miguel Delgado

Instituto de Astrofísica de Canarias, c/ Vía Láctea s/n, E-38205, La Laguna, Tenerife, Spain

`jdelgado@iac.es`

Jesús J. Fuensalida

Instituto de Astrofísica de Canarias, c/ Vía Láctea s/n, E-38205, La Laguna, Tenerife, Spain
Departamento de Astrofísica; Universidad de La Laguna E-38205, La Laguna, Tenerife, Spain

`fuensalida@iac.es`

Marcos Reyes

Instituto de Astrofísica de Canarias, c/ Vía Láctea s/n, E-38205, La Laguna, Tenerife, Spain

`mreyes@iac.es`

Abdelmajid Benhida

High Energy Physics and Astrophysics Laboratory, Université Cadi Ayyad, Faculté des Sciences

Semlalia, Av. Prince My Abdellah, BP 2390 Marrakesh, Morocco

Département de Physique Appliquée, Faculté des Sciences et Techniques, UCAM, BP 549

Marrakesh, Morocco

`benhida@ucam.ac.ma`

Zouhair Benkhaldoun

High Energy Physics and Astrophysics Laboratory, Université Cadi Ayyad, Faculté des Sciences

Semlalia, Av. Prince My Abdellah, BP 2390 Marrakesh, Morocco

`zouhair@ucam.ac.ma`

Diego García Lambas

Instituto de Astronomía Teórica y Experimental, Observatorio Astronómico de la Universidad
Nacional de Córdoba. Laprida 854, Córdoba, Argentina

`dgl@oac.uncor.edu`

Youssef Hach

High Energy Physics and Astrophysics Laboratory, Université Cadi Ayyad, Faculté des Sciences
Semplalia, Av. Prince My Abdellah, BP 2390 Marrakesh, Morocco

`hach-youssef@yahoo.fr`

M. Lazrek

High Energy Physics and Astrophysics Laboratory, Université Cadi Ayyad, Faculté des Sciences
Semplalia, Av. Prince My Abdellah, BP 2390 Marrakesh, Morocco

`lazrek@ucam.ac.ma`

Gianluca Lombardi

European Southern Observatory, Karl-Schwarzschild-Str. 2 - 85748 Garching bei München.
Germany

`glombard@eso.org`

Julio Navarrete

European Southern Observatory, Karl-Schwarzschild-Str. 2 - 85748 Garching bei München.
Germany

`jnavarre@eso.org`

Pablo Recabarren

Instituto de Astronomía Teórica y Experimental, Observatorio Astronómico de la Universidad
Nacional de Córdoba. Laprida 854, Córdoba, Argentina

pablo@oac.uncor.edu

Victor Renzi

Instituto de Astronomía Teórica y Experimental, Observatorio Astronómico de la Universidad
Nacional de Córdoba. Laprida 854, Córdoba, Argentina

vrenzi@oac.uncor.ed

Mohammed Sabil

High Energy Physics and Astrophysics Laboratory, Université Cadi Ayyad, Faculté des Sciences
Semplalia, Av. Prince My Abdellah, BP 2390 Marrakesh, Morocco

sabilmohammed@yahoo.fr

and

Rubén Vrech

Instituto de Astronomía Teórica y Experimental, Observatorio Astronómico de la Universidad
Nacional de Córdoba. Laprida 854, Córdoba, Argentina

rubenv@oac.uncor.ed

Received _____; accepted _____

ABSTRACT

This is the second article of a series devoted to European Extremely Large Telescope (E-ELT) site characterization. In this article we present the main properties of the parameters involved in high angular resolution observations from the data collected in the site testing campaign of the E-ELT during the Design Study (DS) phase. Observations were made in 2008 and 2009, in the four sites selected to shelter the future E-ELT (characterized under the ELT-DS contract): Aklim mountain in Morocco, Observatorio del Roque de los Muchachos (ORM) in Spain, Macón range in Argentina, and Cerro Ventarrones in Chile. The same techniques, instruments and acquisition procedures were taken on each site. A Multiple Aperture Scintillation Sensor (MASS) and a Differential Image Motion Monitor (DIMM) were installed at each site. Global statistics of the integrated seeing, the free atmosphere seeing, the boundary layer seeing and the isoplanatic angle were studied for each site, and the results are presented here. In order to estimate other important parameters such as the coherence time of the wavefront and the overall parameter “coherence étendue” additional information of vertical profiles of the wind speed was needed. Data were retrieved from the National Oceanic and Atmospheric Administration (NOAA) archive. Ground wind speed was measured by Automatic Weather Stations (AWS). More aspects of the turbulence parameters such as their seasonal trend, their nightly evolution and their temporal stability were also obtained and analyzed.

Subject headings: site testing - site characterization

1. Introduction

The site selection for the future large European telescope is a fundamental issue and was undertaken within the E-ELT Design Study proposal funded by the European Community. First meetings and contacts to define the site selection project started in 2003. Possible interested partners and institutions were approached and a first version of design and plans was submitted to the European Commission in February 2004. After revision, using the committee feedback, the final proposal was accepted at the end of 2004. The Site Selection work started formally in 2005 to end in May 2009. In Vernin et al. (2011) (hereafter Paper I) we presented an overview of the campaign.

In the present work the statistics of the parameters relevant to high angular resolution (HAR) astronomy of such a large telescope are presented and discussed in detail. Results were obtained after the analysis of about one year of atmospheric turbulence observations with the same instrumentation (MASS-DIMM, see Kornilov et al. (2007)) in four different sites: Aklim (in Morocco), Macón (in Argentina), Observatorio del Roque de los Muchachos (ORM) (in Spain) and Ventarrones (in Chile). This study is similar to the site characterization produced by the Thirty Meter Telescope (TMT) team: its first article from Schöck et al. (2009) and those focused on the statistics of the seeing and the isoplanatic angle Skidmore et al. (2009), and on the coherence time Travouillon et al. (2009).

The paper is organized as follows: First, the overall observing configuration at each site is detailed in Sec. 1.1 and the definitions of the parameters under study are introduced in Sec. 1.2. The employed instruments and the data provided by them are described in Sec. 2.1, while Sec. 2.2 is devoted to the archives used in order to obtain the complete vertical wind profiles at each site, which are needed to compute some of the parameters. Their main global statistics is covered in Sec. 3. The seasonal behavior, the evolution during an averaged observing night and the stability of the studied atmospheric parameters are addressed, respectively, in Secs. 4, 5 and 6. Finally, the

main results are summarized in Sec. 7.

1.1. Observing configuration

Our aim was to monitor the atmospheric turbulence at the four candidate sites using well-known, reliable and as much homogeneous instrumentation as possible. All the MASS-DIMM instruments were installed on 5 m high towers. This was agreed based on previous studies on the surface layer thickness (see Vernin & Muñoz-Tuñón (1992)). Here follows the instrument setup:

- Four identical MASS-DIMM instruments.
- Four identical telescopes Celestron C11 (11 inches).
- Four identical fast read-out CCDs for DIMM devices: the PCO PixelFly VGA¹.
- Each MASS device contains four photo-multipliers (Kornilov et al. 2007).
- Four towers in order to observe at 5 m above ground level.
- Three robotic mounts (ASTELCO NTM-500²) installed at ORM, Macón and Ventarrones, and one automatic (Losmandy Gemini³) installed at Aklim.
- Four Automatic Weather Stations (AWS) at few meters above ground level (see Paper I for details).

The observations taken at Aklim and ORM sites were carried out regularly by observers (in particular, at ORM site observations took place five nights per week; at Aklim, observations are

¹<http://www.pco.de/sensitive-cameras/pixelfly-vga/>

²<http://www.astelco.com/products/ntm/ntm.htm>

³<http://www.losmandy.com/losmandygoto/gotospecs.html>

less regular due to strong difficulties to access the mountainous site), while those taken at Macón and Ventarrones sites are obtained robotically every night. More details about the duty cycle of the MASS-DIMM instrument in each site was already given in Fig 1 of Paper I.

Concerning the observation itself, the configuration adopted in each site is summarized in Tables 1 and 2. The measurements taken with both instruments, DIMM and MASS, are filtered according to well defined criteria stated in Sec. 2.1.4. After filtering, one obtains the total number of accepted data N_{acc} and the percentage of rejected data N_{rej} . These parameters, together with the total number of exposures per measurement, N_{exp} , the exposure time, t_{exp} and the median sampling time, Δt are given in Tables 1 and 2 for the DIMM and the MASS respectively.

1.2. Parameters

The major parameters relevant to high angular resolution (imaging, adaptive optics, interferometry) have been grouped into two classes: “integrated” parameters and “profiles”. The later class is represented by optical turbulence profiles, $C_N^2(h)$ and wind speed profiles $\mathbf{V}(h)$. It is well known that integrated parameters, such as seeing or Fried’s radius, isoplanatic angle and coherence time, can be deduced from both the above-mentioned profiles as:

- **Fried’s radius:**

$$r_0 = 0.185\lambda^{6/5} \left(\int_0^\infty C_N^2(h) dh \right)^{-3/5} \quad (1)$$

- **Seeing:**

$$\varepsilon_{\text{fwhm}} = 0.98 \frac{\lambda}{r_0} = 5.25\lambda^{-1/5} \left(\int_0^\infty C_N^2(h) dh \right)^{3/5} \quad (2)$$

- **Isoplanatic angle:**

$$\theta_0 = 0.058\lambda^{6/5} \left(\int_0^\infty h^{5/3} C_N^2(h) dh \right)^{-3/5} \quad (3)$$

- **Coherence time:**

$$\tau_0 = 0.058\lambda^{6/5} \left(\int_0^\infty |\mathbf{V}(h)|^{5/3} C_N^2(h) dh \right)^{-3/5} \quad (4)$$

where the light wavelength is $\lambda = 0.5 \mu\text{m}$ and all the measurements are referred to zero zenith angle.

Although seeing is generally considered the most important parameter for HAR astronomy, various combinations of ε , θ , τ are also used to compute some figure of merit, as already discussed by Paper I, depending upon the high angular resolution technique employed. A more general approach is given by Lloyd (2004), who defines the “coherence étendue” G_0 , in which a photon remains coherent. G_0 takes into account a combination of Fried’s radius, isoplanatic angle and coherence time:

$$G_0 = r_0^2 \tau_0 \theta_0^2. \quad (5)$$

This new formulation shows a strong dependence of G_0 with r_0 and θ_0 and less with τ_0 . G_0 is computed with r_0 , τ_0 and θ_0 respectively expressed in m^2 , ms and arcsec^2 .

2. MASS-DIMM and complementary NOAA data

2.1. MASS-DIMM

MASS and DIMM devices are attached to the same equatorial mount and track at the same star, but each instrument has its own setup.

2.1.1. Differential Image Motion Monitor (DIMM)

DIMM provides accurate, absolute and reproducible integrated seeing data although systematic control tests on the focus or saturation are however important (see e.g. Tokovinin

2002; Varela et al. 2004). The instrument description is given in Sarazin & Roddier 1990 and Vernin & Muñoz-Tuñón 1995. Since the early nineties, DIMMs have become very popular and have been used at different observatories. DIMMs are now auxiliary instruments for telescope operation and complement Adaptive Optics (AO) experiments. For what concerns the site selection, accurate statistics is an important issue. A lot of results have been recorded in large databases that can be available in Muñoz-Tuñón et al. 1997; Ehgamberdiev et al. 2000. For example, in Ehgamberdiev et al. 2000 seeing values at Paranal and La Palma were analyzed and compared for more than two years. From this analysis, the excellent behavior of the two sites is clear and reinforces their pre-selection for hosting the future E-ELT. But the DIMM provides only the seeing, and a $C_N^2(h)$ profile is needed to access the isoplanatic angle (Eq. 3).

2.1.2. Multi-Aperture Scintillation Sensor (MASS)

This instrument detects fast intensity variations of light in four concentric apertures using photo-multipliers. Every minute, the accumulated photon counts obtained with micro-exposures of 1 ms are converted to four normal scintillation indices and to six differential indices for each pair of apertures. This set of ten numbers is fitted by a model of six thin turbulent layers at pre-defined altitudes, $h_i = 0.5, 1, 2, 4, 8,$ and 16 km above the site altitude (Kornilov et al. 2003). Another model of three layers at *floating* altitudes is fitted as well. The set of integrals of the refractive index structure constant,

$$J_i = \int_{i\text{th layer}} C_N^2(h)dh, \quad (6)$$

in these six (or three) layers represent the optical turbulence profiles measured by MASS (see Tokovinin et al. (2003) for details on MASS weighting functions). Turbulence near the ground does not produce any scintillation: MASS is *blind* to it and can only measure the seeing in the free atmosphere.

MASS has been cross-compared with the Generalized SCIntillation Detection And Ranging (G-SCIDAR) optical turbulence profiler (Avila et al. 1997), during a campaign performed at Mauna Kea (Tokovinin et al. 2005) showing very good agreement. SCIDAR has proved to be the most efficient and reliable technique to accurately measure the optical vertical structure of the atmospheric turbulence strength from ground level, although it requires a one-meter class telescope to perform the observations. A more recent study carried out at Paranal Observatory (Dali Ali et al. 2010) also produced consistent results. Similar comparisons between the parameters provided by the MASS-DIMM instrument and the G-SCIDAR, made at ORM, will be addressed in the forthcoming issue within the present series which will be devoted to the G-SCIDAR profiles.

Assuming that the optical turbulence profile remains constant within each slab defined by the MASS, one can deduce the isoplanatic angle (Eq. 3). The coherence time (Eq. 4) still requires the knowledge of the wind speed profile which is not delivered by the MASS, but will be retrieved from meteorological archives, as explained in Sec. 2.2.

2.1.3. *Cross-calibration of the DIMM device*

This section describes the comparison made between the seeing values obtained with one of the DIMM devices employed during the E-ELT site characterization project (the DIMM part of the MASS-DIMM instrument) and with an existing stable seeing monitor at ORM (hereafter called IAC-DIMM, Vernin & Muñoz-Tuñón 1995). An on-line report is available⁴ with detailed information on the systems setup and on data analysis that is not included in this section.

The campaign took place for four nights in September 2007, a few months before the starting of the turbulence monitoring runs, with both instruments, the E-ELT and IAC DIMMs, located at

⁴http://www.iac.es/proyecto/site-testing/index.php?option=com_content&task=view&id=7

ground level and at a distance of four meters from each other.

Although the telescope apertures are not the same (the IAC-DIMM is 8" while the other is 11") the combination of telescope and CCD gave rise to a very similar pixel scales, around $0.8 \text{ arcsec pix}^{-1}$. They were empirically measured through the observation of a double star with known angular separation. So, similar performances of both systems were expected. The study was restricted to the observation of the same stars by both instruments and at the same time. The targets were selected to be as close as possible to the zenith.

Both seeing time series followed a similar behavior. The differences between the seeing values measured by the E-ELT DIMM and those of the IAC-DIMM $\varepsilon_{\text{ELT-DS}} - \varepsilon_{\text{IAC-DIMM}}$ had a mean value of 0.035 arcsec, a median of 0.037 arcsec and a standard deviation of 0.099 arcsec.

As a result, seeing values provided by the E-ELT site characterization DIMM device are in good agreement with those of IAC-DIMM within the measured range: from $\varepsilon \simeq 0.3 \text{ arcsec}$ to $\varepsilon \simeq 1.1 \text{ arcsec}$. This is shown in Figure 1, where the IAC-DIMM data are plotted versus those acquired by the ELT-DS DIMM. A linear fit, $y = Bx + A$ with the condition $A = 0$, yields a slope very close to the unity, $B = 1.01 \pm 0.01$. Unfortunately, bad seeing values (those worse than 1 arcsec) were scarce and therefore were not well sampled during that four nights of cross-calibration.

2.1.4. Data rejection

Raw data provided by each instrument are validated and filtered following standard criteria. In the case of DIMM device, following Muñoz-Tuñón et al. 1997, the longitudinal $FWHM_\ell$ and the transverse $FWHM_t$ seeing are compared so that only data fulfilling (Eq. 7) are taken into account:

$$0.8 < \frac{FWHM_\ell}{FWHM_t} < 1.2. \quad (7)$$

The reason for rejection comes from the physics bases of the DIMM technique (see the study on its uncertainties and errors made by Vernin & Muñoz-Tuñón (1995)) and ensures the reliability of the measurements.

For what concern the MASS device, several parameters such as the removal of vignettted data and the correction of MASS overshoot are taken into account. All them are inspired by the work of Kornilov et al. 2007. The flux recorded by the MASS D channel F_D and its background signal B_{F_D} are used to check the signal-to-noise ratio. Uncertainty of the free atmosphere seeing ε_{fa} provided by the MASS software is also used as test value. Finally, the chi-square corresponding to the restoration of the $C_N^2(h)$ profile is also taken into account. The adopted criteria for MASS accepted measurements are the following:

- Prevents too faint star or clouds: $B_{F_D} < 3\%$ and $F_D > 100$ pulses/ms.
- Prevents too bright sky: relative F_D error ≤ 0.03 .
- $\sigma_{\varepsilon_{\text{fa}}} < 0.15$ arcsec.
- Prevents bad profile restoration: from restored $C_N^2(h)$ profile, $\chi^2 < 100$.

2.1.5. *Boundary layer contribution*

The boundary layer seeing ε_{bl} , here defined as the integrated turbulence between $h = 5$ m and $h = 500$ m, is evaluated from combined MASS-DIMM observations, as follows:

$$\varepsilon_{\text{bl}}^{5/3} = \varepsilon^{5/3} - \varepsilon_{\text{fa}}^{5/3} \quad (8)$$

where ε is the value provided by the DIMM and ε_{fa} is gathered by integrating the MASS profiles. Due to noise, it may happen that doing the subtraction in (Eq. 8) the boundary layer seeing is negative, and it is withdrawn from the statistics. We estimated that, so doing, any possible bias is almost negligible because it happened very seldom at ORM (2.8% of the whole data set), Aklim (3.8%) and Ventarrones (7.8%). However, at Macón this happened more often (17.6%), mainly during the southern winter (from August to November) coinciding with very strong wind regimes. It turned out that the percentage of this anomalies increases with the free atmosphere seeing, so rejecting those data means biasing to lower ε_{fa} . Around the southern summertime, when the wind speed was lower than in winter but still higher compared to the other three sites, the percentages of these occurrences falls from more than 25% to around 13% of the total data acquired. See the next forthcoming issue of this series of papers, which will be devoted to ground meteorology, for a more detailed discussion.

2.2. **Complementary wind speed data**

As expressed in Sec. 1.2 and (Eq. 4), wind speed profiles are mandatory to access the coherence time and MASS-DIMM cannot provide these missing data. Travouillon et al. 2009 wrote a long discussion about the possibility to retrieve τ_0 with the MASS only, according to a

Tokovinin document ⁵, but still leading to uncertainties of up to 20%.

In order to retrieve the missing wind speed profiles necessary to solve (Eq. 4), we extracted them from Air Resources Laboratory (ARL) of the National Oceanic and Atmospheric Administration (NOAA) archive⁶, from Global Data Assimilation System (GDAS) database, with a 1° horizontal resolution and a 3 hour temporal resolution. At ground level, we used wind speed given by our Automatic Weather Stations (AWS). Wind profiles have a sampling rate of 3 hours. In order to compare them with the MASS, DIMM and AWS databases, few assumptions were necessarily adopted: 1) The NOAA/ARL wind speed profiles were considered constant from 1.5 hours before and after the $V(h)$ time stamp. At ground level, wind speed is obtained from the AWS (at 2 m at Aklim and at 10 m elsewhere) to complete the vertical wind profile. 2) MASS sensitivity function, which approximately consists on triangular functions whose peaks are distributed on a 2^n logarithmic scale (at 0.5, 1, 2, 4, 8 and 16 km), is applied to $V(h)$ profile in order to obtain the wind speed at the layers defined by MASS instrument. 3) Value of $C_N^2(h)$ corresponding to the first 500 m, which is not reachable by the MASS, were obtained through the combination of the information provided by DIMM (the total atmosphere seeing) and MASS (the free atmosphere seeing and the and the $C_N^2(h)$ from $h = 500$ m above). With all this information that involves measurements of DIMM, MASS, AWS and NOAA/ARL wind profiles, τ_0 can be estimated (see (Eq. 4)). Once τ_0 is obtained, the *coherence étendue* G_0 can be computed (Eq. 5).

3. Global statistics

In this section, the statistics of seeing (ε), isoplanatic angle θ_0 , coherence time τ_0 , “coherence étendue” G_0 , Fried’s radius (r_0), free atmosphere seeing ε_{fa} , boundary layer seeing ε_{bl} , at each of

⁵www.ctio.edu/atokovinin/profiler/timeconst.pdf

⁶<http://www.arl.noaa.gov/READYamet.php>

the four sites: Aklim, Macón, ORM and Ventarrones sites is presented.

Data processing software has been implemented by IAC team and we made it available to all institutions who take care of data gathering and analysis at the different sites (see Paper I). Statistics of the above mentioned parameters are obtained from the whole data set and according to the previous remarks concerning the turbulence within the boundary layer and the wind profiles. From the probability distribution of each parameter the cumulative distribution and four percentiles: 0.05, 0.25, 0.75 and 0.95 were computed together with the mean, the standard deviation of the mean and the median (0.50 percentile) of the corresponding data subset.

Many properties of these parameters might be analyzed depending on each possible purpose, such as the trend of the parameters along a year (Sec. 4), their typical behavior during the night (Sec. 5) and their temporal stability (Sec. 6). The global statistics only takes into account the valid data (those that fulfill the criteria mentioned in Sec. 2.1.4) as a whole, regardless of any temporal consideration. The global statistics of the parameters ε , θ_0 , τ_0 , G_0 , r_0 , ε_{fa} and ε_{bl} are presented in Tables 3 and 4 over the whole observing campaign at the four sites. Both tables show the median, the mean, the standard deviation of the mean, σ , four percentiles, 5%, 25%, 75% and 95%, the number of accepted data N_{acc} , as well as the percentage of rejected data, in accordance to the criteria mentioned in Sec. 2.1.4, and the total of continuous observing hours, t_{obs} , for each parameter and at each site.

Notice in Table 3 that the number of τ_0 and G_0 measurements corresponding to Aklim site is much less than those of the other three sites. The reason for so extremely low number of data for these parameters in Aklim comes from the sampling of its AWS. As already mentioned in Sec. 2.2, the τ_0 computation (so, also G_0 's) requires the wind speed at ground level acquired by the AWS and, while for the other three sites their sampling is a record per minute, at Aklim it is only one record every five minutes. This led to the aforementioned poorer statistics.

The summary of the best achieved values of the different parameters at the different sites is

the following:

During the extend of the E-ELT site campaign, the lowest median integrated seeing was obtained at ORM ($\varepsilon = 0.80$ arcsec). If this particular value is compared with the results of the TMT site testing campaign, it is found that it is around 0.1 arcsec higher than those obtained at the TMT candidate sites showing the best total seeing statistics (see Skidmore et al. (2009)). However, in the particular case of the ORM, for instance, previous studies have proven that they are very similar (see e.g. Muñoz-Tuñón et al. (1997)). The best median isoplanatic angle was very similar both at Ventarrones and at ORM ($\theta_0 \simeq 2$ arcsec) and they are comparable to most of those found in the TMT candidate sites, except Mauna Kea, which benefits from a better isoplanatic angle ($\theta_0 = 2.69$ arcsec) (Skidmore et al. 2009). The best (highest) median coherence time was measured at ORM ($\tau_0 = 5.58$ ms), closely followed by Ventarrones, and both of them better ($\tau_0 \gtrsim 5$ ms) than at Aklim and Macón ($\tau_0 \approx 3.5$ ms). The τ_0 values at ORM and Ventarrones are also comparable to those of the candidate sites of the TMT with highest coherence time, τ_0 better than 5 ms (see Travouillon et al. (2009)). Finally, the combined parameter G_0 defined in (Eq. 5) was clearly higher at ORM ($G_0 = 0.4 \text{ m}^2 \text{ ms arcsec}^2$) and Ventarrones ($G_0 = 0.3 \text{ m}^2 \text{ ms arcsec}^2$) than at Macón and Aklim ($G_0 \simeq 0.1 \text{ m}^2 \text{ ms arcsec}^2$).

The smallest contribution of the free atmosphere measured by the MASS instrument was obtained again at ORM ($\varepsilon_{\text{fa}} = 0.31$ arcsec) although the median contribution of the boundary layer measured was lower at Macón ($\varepsilon_{\text{bl}} = 0.51$ arcsec) and at Ventarrones ($\varepsilon_{\text{bl}} = 0.60$ arcsec) than at ORM ($\varepsilon_{\text{bl}} = 0.65$ arcsec). The relative contribution of the ground layer and the free atmosphere to the total seeing at each site is shown in Table 5. In this regard, a turbulence profile showing a higher proportion of boundary layer turbulence, with a relatively clear free atmosphere, will be much more tractable for an adaptive optics system than one with, for example, strong jet stream-related turbulence in the tropopause (see e.g. Marks (2002); Vernin & Muñoz-Tuñón (1994)).

In Figures 2 to 7, the histogram as well as the cumulative distribution of seeing ε , isoplanatic angle θ_0 , coherence time τ_0 , "coherence étendue" G_0 , free atmosphere seeing ε_{fa} and boundary layer seeing ε_{bl} , again, at each of the four sites are plotted. As it is well known, the conditions, in terms of atmospheric turbulence, are more favorable when some parameters are small: seeing (integrated, free atmosphere and boundary layer) or/and when they are large: isoplanatic angle, coherence time, Fried's radius and "coherence étendue". In the last cases (θ_0 , τ_0 , r_0 and G_0) instead of estimating the cumulative distribution, the complementary cumulative distribution is calculated, which equals 1 minus the cumulative distribution, and is drawn in blue rather than in red in the plots. The four percentiles and the median are indicated by dotted lines, while the mean is marked with a dashed one in each of the figures.

As a summary, the cumulative distributions of the four candidate sites were put together in a plot for each parameter in Figure 8. From these cumulative distributions at the different sites it is concluded that ORM shows the best behavior in all the values ε , θ_0 , τ_0 and G_0 , closely followed by Ventarrones.

4. Seasonal evolution

Although the length of the FP6 campaign is only slightly longer than a year, the monthly variations of the quantities under consideration are shown in Figures 9 and 10; in particular, the statistics of the parameters ε , θ_0 , τ_0 , G_0 , ε_{fa} and ε_{bl} are presented for each month along the whole observing campaign at the four sites. Surprisingly, the seeing seems better (lower) during May-Aug 2008 and Jan-Apr 2009, in both hemispheres, when one would expect an inverse trend depending on the hemisphere. In large database studies, e.g. at ORM, the seasonal trend is more remarked, with summer being the best period (Muñoz-Tuñón et al. 1997). We conclude that this one-year is not enough for study the seasonal evolution.

5. Evolution during the night

Nightly evolution of ε , θ_0 , τ_0 , G_0 , ε_{fa} and ε_{bl} at each of the four sites, over the whole campaign is plotted in Figures 11 to 16. Mid-line represent the middle of the astronomical night (the middle point between sunset and sunrise). Due to the fact that the length of the night varies during the year, the beginning and the end of the figures are worse sampled than around the astronomical midnight (this is shown with a black curve in the plots). Every quarter of an hour, before and after midnight, all the data have been averaged in order to put into evidence any trend during the night. No clear nightly trend is visible except perhaps at Macón site where the conditions are poor at the beginning of the night (large seeing, low isoplanatic angle, small coherence time and thus, low "coherence étendue", and they get gradually better during the night until the sunset. This behavior is highly correlated with the evolution of wind speed at Macón, being high at the sunset and decreasing along the night. This issue will be discussed in more detail in the next paper dedicated to meteorological statistics.

6. Temporal stability

In Figure 17 is drawn the "stability" of each of the following parameters, ε , θ_0 , τ_0 , G_0 , ε_{fa} and ε_{bl} . Stability means the average of the time interval during which a parameter, say seeing, remains "better" than a given value. This means, in some cases, to be lower than that value (integrated seeing, free atmosphere seeing and boundary layer seeing) and in other cases to be higher (isoplanatic angle, coherence time and "coherence étendue"). The stability plots were build assuming a threshold of 4 min in order to decide whether two consecutive data points of the time series are considered belonging to the same time interval or, on the contrary, the continuity has been broken. The time intervals during which each parameter remains below (or above) a given value were averaged. This procedure leads to the smooth curves shown in Figure 17.

This concept is important to get an idea of how many time the atmospheric conditions would remain stable in order to carry out a particular observation that may imply a specific adaptative optics configuration. As an overall result, ORM site seems to exhibit higher stability than the three other sites, except for what concern isoplanatic angle.

7. Summary

The FP6 site testing campaign for the E-ELT measurements started in April 2008 and finished in May 2009. Four sites were characterized: Aklim (in Morocco), Macón (in Argentina), ORM (in Spain) and Ventarrones (in Chile). The observations were made under almost identical instrumentation and setup for data analysis homogeneity. The main statistical properties of the parameters were discussed here. The study is limited to the observations made during the FP6 contract.

In this sense, it is clear that a longer campaign would have been desirable in order to get rid of any bias produced by peculiar conditions during particular periods of time within the observations. A longer campaign would have made the conclusions of this study more robust. Unfortunately, the time spent to setup the systems in the four sites and the time constrains naturally associated to the ELT-DS work package resulted in a campaign slightly longer than one year. In any case, detailed and valuable information on these sites is provided here. Data and results from the E-ELT site study can be put in a more general context by making use of longer databases, when available, at the different sites.

The parameters relevant for performing high angular resolution observations were obtained employing several instruments (MASS-DIMM and AWS installed in each of the four candidate sites) and the NOAA/ARL wind profile database (needed to determine the coherence time). Data coming from the MASS-DIMM instruments was carefully filtered by means of standard and

well-known criteria in order to get rid of spurious data. The DIMM instrument measurements were compared with a stable IAC DIMM at ORM for several night finding satisfactory correlation between them.

In the case of the reference sites, ORM and Ventarrones (some kilometers away from Paranal Observatory), there exist large records of atmospheric turbulence conditions, although the discussion here is limited to the results of the FP6 contract campaign. However, it is worth noting that, the present work represent the first results obtained at the *new* sites Aklim and Macón.

The global statistics of the high angular resolution parameters were studied as well as their seasonal trend, their evolution during a typical night and their time stability.

Concerning pure statistics, the following are the ranges of the median values taken by the studied parameters during the campaign: the integrated seeing, ε , from 0.80 arcsec (ORM) to 1.00 arcsec (Aklim); the isoplanatic angle, θ_0 , from 1.29 arcsec (Aklim) to $\theta_0 \approx 2$ arcsec (Ventarrones and ORM); the coherence time, τ_0 , from 3.37 ms (Macón) to 5.58 ms (ORM); the coherence *étendue*, G_0 , from $0.05 \text{ m}^2 \text{ ms arcsec}^2$ (Aklim) to $0.38 \text{ m}^2 \text{ ms arcsec}^2$ (ORM); the Fried's radius, r_0 , from 10.1 cm (Aklim) to 12.7 cm (ORM); the free atmosphere seeing, ε_{fa} , from 0.31 arcsec (ORM) to 0.66 arcsec (Macón); and the boundary layer seeing ε_{bl} , from 0.51 arcsec (Macón) to 0.77 arcsec (Aklim). Moreover, the percentages of the contribution of the boundary layer seeing to the total atmosphere seeing were 71% (ORM), 65% (Aklim), 50% (Ventarrones) and 41% (Macón). Both reference sites, ORM and Ventarrones, presented significantly higher median values of the global parameter $G_0 = 0.4 \text{ m}^2 \text{ ms arcsec}^2$ and $G_0 = 0.3 \text{ m}^2 \text{ ms arcsec}^2$ respectively, than those found at Aklim and Macón, with $G_0 \approx 0.1 \text{ m}^2 \text{ ms arcsec}^2$.

The site testing campaign lasted for around a year so, although the monthly values of every parameter were estimated in order to study their behavior along the year, more observations would be obviously needed to make conclusions about seasonal trends of the sites under consideration.

Regarding the trend of the parameters averaged over all observation nights, it is found that they are very stable in ORM and Ventarrones sites. Aklim also showed good stability along the night, although most of the parameters seem to behave slightly better during the second half of the night than during the first half. A systematic variation was identified at Macón site, where the observing conditions are poor at the beginning and they get gradually better, being this phenomenon correlated with strong winds at the beginning getting weaker to sunset.

The temporal stability of the parameters was also investigated. ORM showed generally better stability than the other three sites. As an example, the total seeing remained below 1 arcsec, the free atmosphere seeing below 0.5 arcsec, the isoplanatic angle was higher than 1.5 arcsec and the coherence time was higher than 5 ms for an hour, on average, at ORM (all these parameters considered separately; i.e. these conditions not necessarily occurring at the same time).

8. Acknowledgements

We acknowledge the European Community which granted this ELT Design Study in the Framework Programme 6 (Contract 11863). We thank R. Gilmozzi, Principal Investigator of the E-ELT project, for his help, and also the ESO members who participated in the organization of many international meetings. We are grateful to P. Bonet, S. Rueda, J. Rojas, to the technicians in telescope operations and to many of the technicians of the IAC for performing the observations and for their technical support at ORM; and also our acknowledgments to the observers at Paranal for their help and observations during the Cute-Scidar campaigns. Moroccan team are grateful to the Moroccan Hassan II Academy of Science and Technology, which financially supported the site testing campaigns at the Aklim site. Our sincere gratitude also goes to the site surveyors and to all the staff members for their help and dedication, in particular: A. Habib, A. Jabiri, A. Bounhir and the 3AM staff. We acknowledge also Hernan Muriel, Diego Ferreira, Federico Staszczyn and Jose Viramonte for their help at Macon. We are indebted to NOAA-ARL administration which supplies

free meteorological archives helping us to compute some of the parameters included in this study. We also thank the anonymous referee for useful comments that improved the manuscript.

REFERENCES

- Avila, R., Vernin, J., & Masciadri, E. 1997, *Appl. Opt.*, 36, 7898
- Dali Ali, W., et al. 2010, *A&A*, 524, A73
- Ehgamberdiev, S. A., Baijumanov, A. K., Ilyasov, S. P., Sarazin, M., Tillayev, Y. A., Tokovinin, A. A., & Ziad, A. 2000, *A&AS*, 145, 293
- Kornilov, V., Tokovinin, A., Shatsky, N., Voziakova, O., Potanin, S., & Safonov, B. 2007, *MNRAS*, 382, 1268
- Kornilov, V., Tokovinin, A. A., Vozyakova, O., Zaitsev, A., Shatsky, N., Potanin, S. F., & Sarazin, M. S. 2003, in *Society of Photo-Optical Instrumentation Engineers (SPIE) Conference Series*, ed. P. L. Wizinowich & D. Bonaccini, Vol. 4839, 837
- Lloyd, J. P. 2004, in *Society of Photo-Optical Instrumentation Engineers (SPIE) Conference Series*, ed. W. A. Traub, Vol. 5491, 190
- Marks, R. D. 2002, *A&A*, 385, 328
- Muñoz-Tuñón, C., Vernin, J., & Varela, A. M. 1997, *A&AS*, 125, 183
- Sarazin, M., & Roddier, F. 1990, *A&A*, 227, 294
- Schöck, M., et al. 2009, *PASP*, 121, 384
- Skidmore, W., Els, S., Travouillon, T., Riddle, R., Schöck, M., Bustos, E., Seguel, J., & Walker, D. 2009, *PASP*, 121, 1151
- Tokovinin, A. 2002, *PASP*, 114, 1156
- Tokovinin, A., Kornilov, V., Shatsky, N., & Voziakova, O. 2003, *MNRAS*, 343, 891
- Tokovinin, A., Vernin, J., Ziad, A., & Chun, M. 2005, *PASP*, 117, 395

- Travouillon, T., Els, S., Riddle, R. L., Schöck, M., & Skidmore, W. 2009, PASP, 121, 787
- Varela, A. M., Muñoz-Tuñón, C., & Vernin, J. 2004, in Society of Photo-Optical Instrumentation Engineers (SPIE) Conference Series, ed. A. L. Ardeberg & T. Andersen, Vol. 5382, 656
- Vernin, J., & Muñoz-Tuñón, C. 1992, A&A, 257, 811
- Vernin, J., & Muñoz-Tuñón, C. 1994, A&A, 284, 311
- Vernin, J., & Muñoz-Tuñón, C. 1995, PASP, 107, 265
- Vernin, J., et al. 2011, PASP, 123, 1334

Table 1: Synthesis of DIMM data acquisition. The number of accepted data, N_{acc} , the percentage of rejected from the total, $N_{\text{rej}}(\%)$, the exposure time t_{exp} , the median time interval between measurements, Δt , and the number of exposures per measurement, N_{exp} , are shown.

DIMM					
site	N_{acc}	$N_{\text{rej}} (\%)$	$t_{\text{exp}} (\text{ms})$	$\Delta t (\text{s})$	N_{exp}
Aklim	10992	21.4	5	42	200
Macón	29723	24.4	5	100	400
ORM	47328	11.3	5	47	200
Ventarrones	56547	8.8	5	101	400

Table 2: Synthesis of MASS data acquisition. The number of accepted data, N_{acc} , the percentage of rejected from the total, $N_{\text{rej}}(\%)$, the exposure time t_{exp} and the median time interval between measurements, Δt are shown.

MASS				
site	N_{acc}	$N_{\text{rej}} (\%)$	$t_{\text{exp}} (\text{ms})$	$\Delta t (\text{s})$
Aklim	13763	25.2	1	63
Macón	94623	5.3	1	63
ORM	35962	15.4	1	63
Ventarrones	83273	1.9	1	63

Table 3:: ε , θ_0 , τ_0 and G_0 statistics obtained from April 2008 to May 2009. The median, the mean, the standard deviation of the mean, four percentiles, the number of accepted data, the % of rejected data and the total observing time are shown.

ε (arcsec)	med	mean	σ	5%	25%	75%	95%	N_{acc}	%rej	t_{obs} (h)
Aklim	1.00	1.09	0.45	0.61	0.81	1.28	1.82	10992	21.4	250
Macón	0.87	0.91	0.26	0.57	0.74	1.05	1.38	29723	24.4	1246
ORM	0.80	0.94	0.55	0.46	0.62	1.06	2.00	47328	11.3	790
Ventarrones	0.91	0.96	0.29	0.58	0.76	1.10	1.50	56547	8.8	2214
θ_0 (arcsec)	med	mean	σ	5%	25%	75%	95%	N_{acc}	%rej	t_{obs} (h)
Aklim	1.29	1.43	0.75	2.66	1.79	0.96	0.55	13763	25.2	296
Macón	1.37	1.51	0.77	2.81	1.85	1.01	0.66	94623	5.3	1705
ORM	1.93	2.02	0.77	3.41	2.44	1.48	0.87	35962	15.4	669
Ventarrones	1.96	2.18	1.92	3.97	2.56	1.47	0.84	83273	1.9	2626
τ_0 (ms)	med	mean	σ	5%	25%	75%	95%	N_{acc}	%rej	t_{obs} (h)
Aklim	3.53	5.64	4.98	15.87	7.46	2.34	1.59	1004	0.0	80
Macón	3.37	3.95	2.67	8.58	4.99	2.20	1.28	69376	1.5	1227
ORM	5.58	6.51	4.14	14.24	8.26	3.70	1.82	36802	0.0	619
Ventarrones	4.90	5.65	4.38	11.77	7.13	3.27	1.58	103782	1.0	1807
G_0 (m ² ms arcsec ²)	med	mean	σ	5%	25%	75%	95%	N_{acc}	%rej	t_{obs} (h)
Aklim	0.05	0.32	0.66	1.71	0.31	0.02	0.01	1004	0.0	80
Macón	0.10	0.35	1.20	1.49	0.30	0.03	0.01	69376	1.5	1227
ORM	0.38	1.02	1.80	4.24	1.16	0.11	0.01	36794	0.0	619
Ventarrones	0.26	0.68	1.42	2.58	0.68	0.09	0.01	103782	1.0	1807

Table 4:: Statistics of r_0 , ε_{fa} and ε_{bl} obtained from April 2008 to May 2009. The median, the mean, the standard deviation of the mean, four percentiles, the number of accepted data, the % of rejected data and the total observing time are shown.

r_0 (cm)	med	mean	σ	5%	25%	75%	95%	N_{acc}	%rej	t_{obs} (h)
Aklim	10.10	10.49	6.43	16.49	12.40	7.92	5.55	10992	21.4	250
Macón	11.56	11.89	3.18	17.74	13.75	9.63	7.33	29723	24.4	1246
ORM	12.71	13.07	5.04	21.87	16.37	9.55	5.06	47328	11.3	790
Ventarrones	11.12	11.48	3.30	17.41	13.37	9.16	6.72	56547	8.8	2214
ε_{fa} (arcsec)	med	mean	σ	5%	25%	75%	95%	N_{acc}	%rej	h_{obs}
Aklim	0.52	0.63	0.39	0.22	0.35	0.77	1.41	13763	25.2	296
Macón	0.66	0.79	0.52	0.25	0.43	0.98	1.83	94623	5.3	1705
ORM	0.31	0.41	0.38	0.14	0.22	0.46	0.97	35962	15.4	669
Ventarrones	0.55	0.65	0.39	0.24	0.38	0.79	1.43	83273	1.9	2626
ε_{bl} (arcsec)	med	mean	σ	5%	25%	75%	95%	N_{acc}	%rej	h_{obs}
Aklim	0.77	0.84	0.38	0.34	0.60	1.00	1.54	5596	3.8	136
Macón	0.51	0.52	0.21	0.20	0.39	0.64	0.86	22189	17.6	976
ORM	0.65	0.74	0.40	0.31	0.48	0.89	1.47	37624	2.8	637
Ventarrones	0.60	0.63	0.26	0.27	0.46	0.78	1.09	52057	7.8	2071

Table 5: Relative contribution of the boundary layer and the free atmosphere to the total seeing at the different sites (obtained using the median values also shown in the table). Sampling period from April 2008 to May 2009.

Site	ε_{bl} (arcsec)	%	ε_{fa} (arcsec)	%	total ε (arcsec)
Aklim	0.77	65	0.52	34	1.00
Macón	0.51	41	0.66	63	0.87
ORM	0.65	71	0.31	21	0.80
Ventarrones	0.60	50	0.55	43	0.91

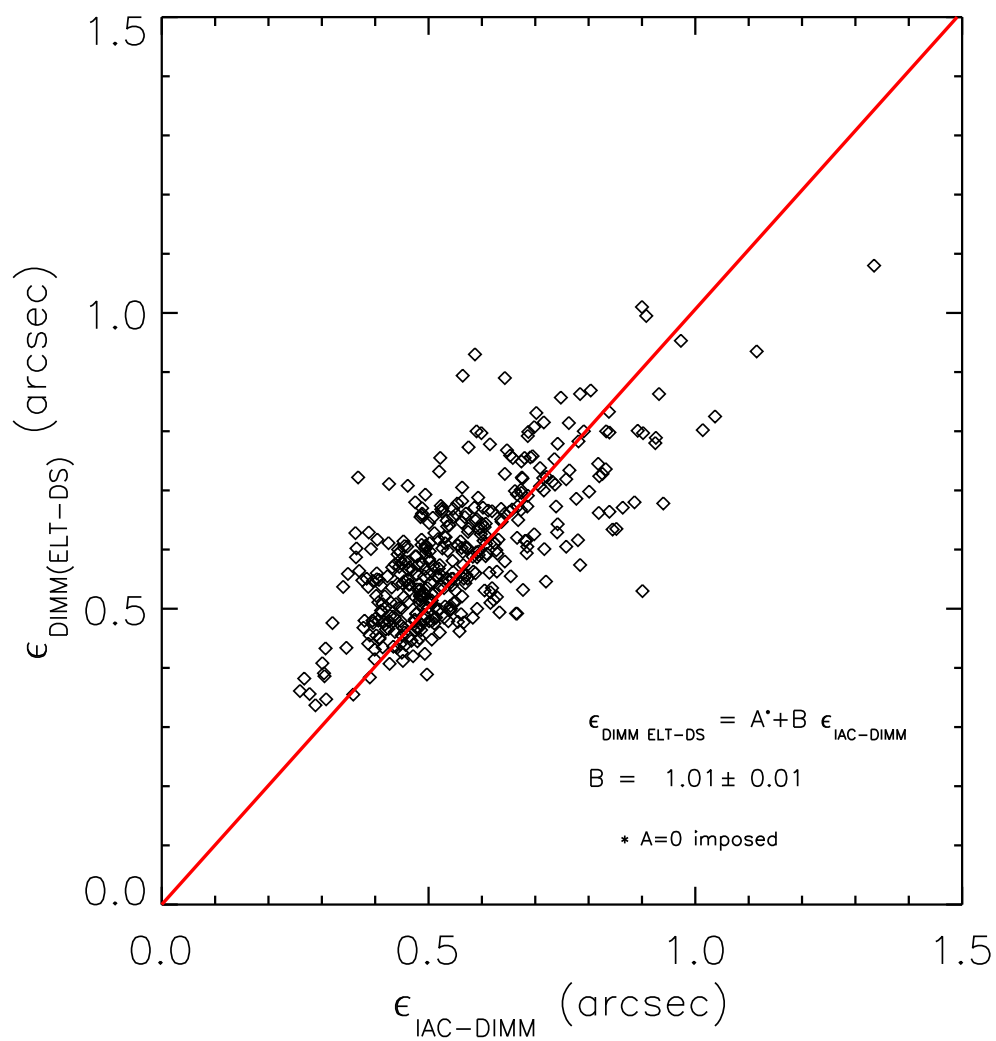


Fig. 1.— Seeing values measured by IAC-DIMM vs those of the DIMM part of the MASS-DIMM device employed for the E-ELT site characterization. The red line is a linear fit with the condition $A=0$, leading to a 1.01 slope.

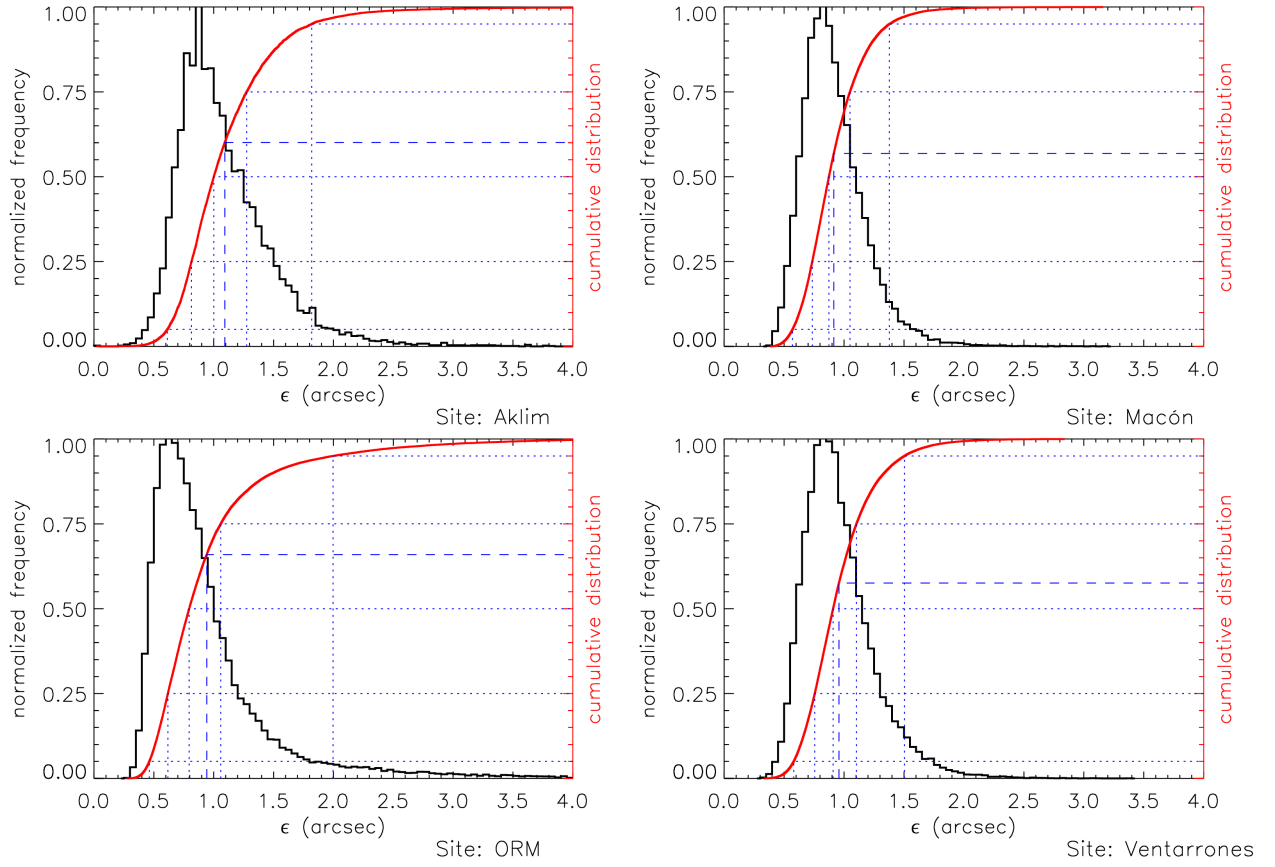


Fig. 2.— Histogram and cumulative distribution of the seeing at each of the four sites.

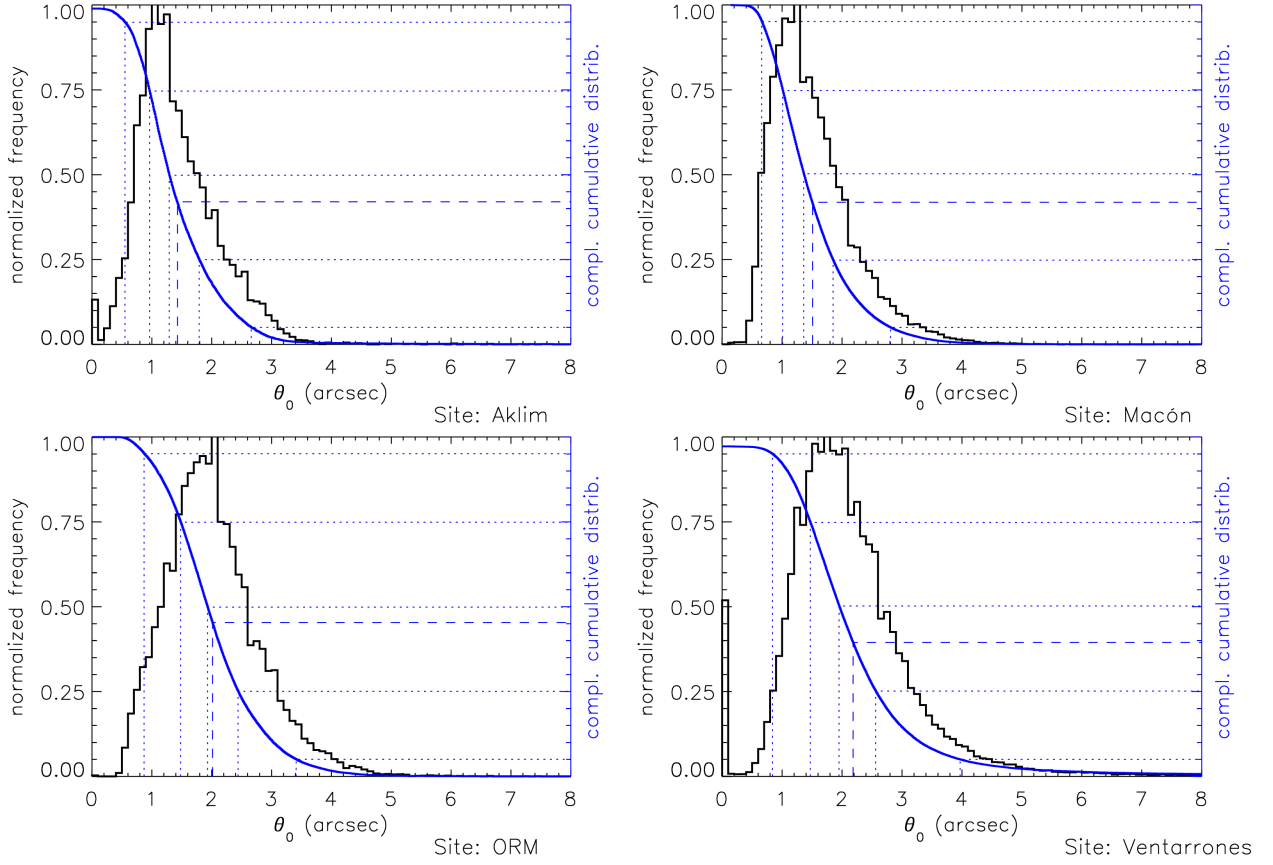


Fig. 3.— Histogram and cumulative distribution of the isoplanatic angle at each of the four sites.

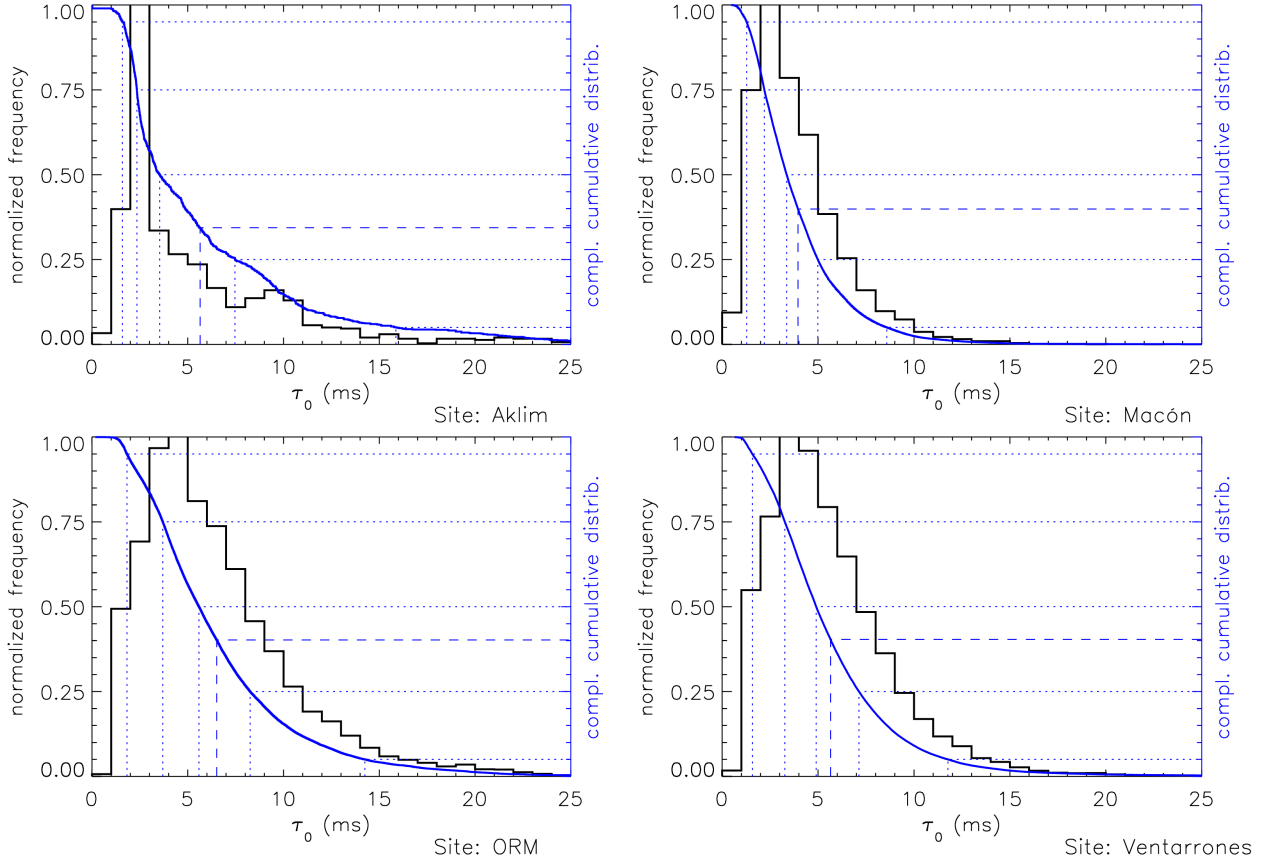


Fig. 4.— Histogram and cumulative distribution of the coherence time at each of the four sites.

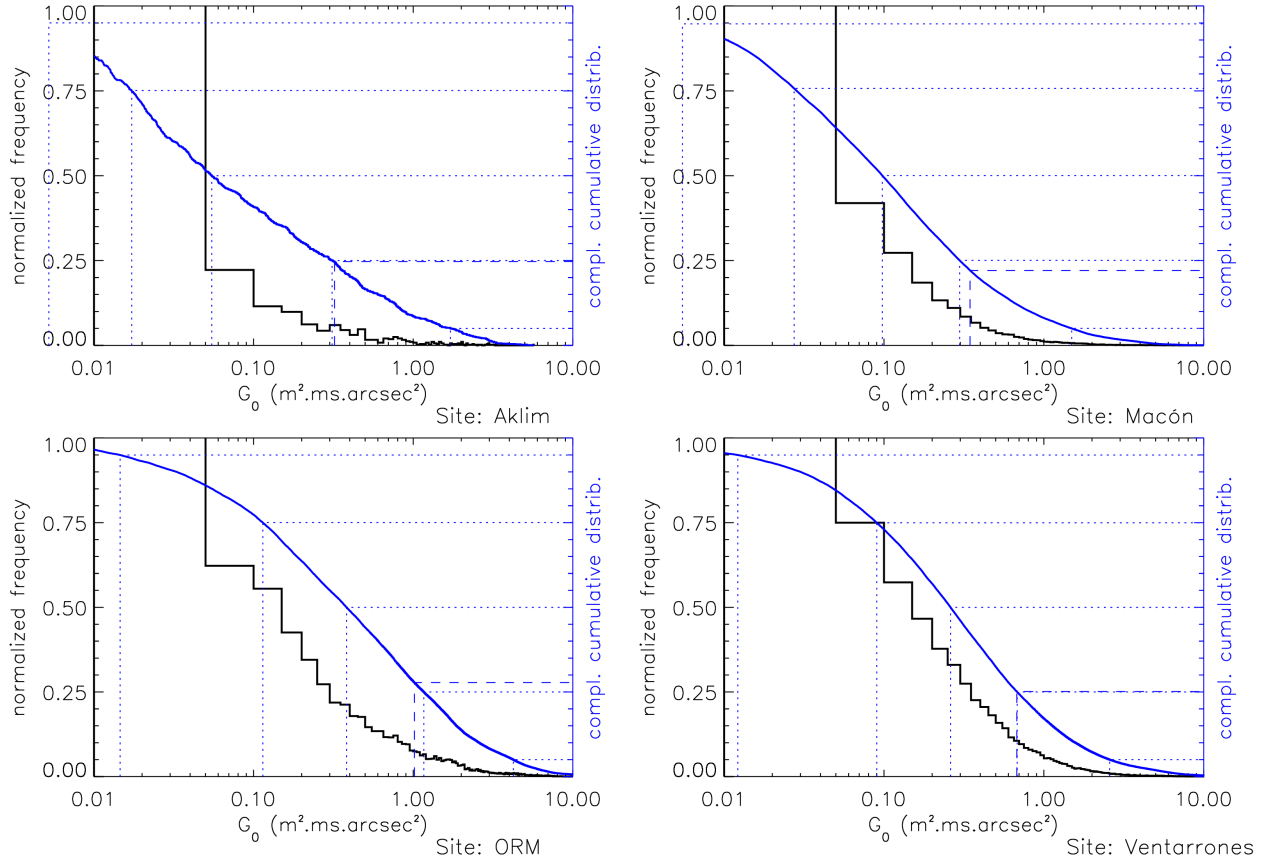


Fig. 5.— Histogram and cumulative distribution of the coherence étendue at each of the four sites.

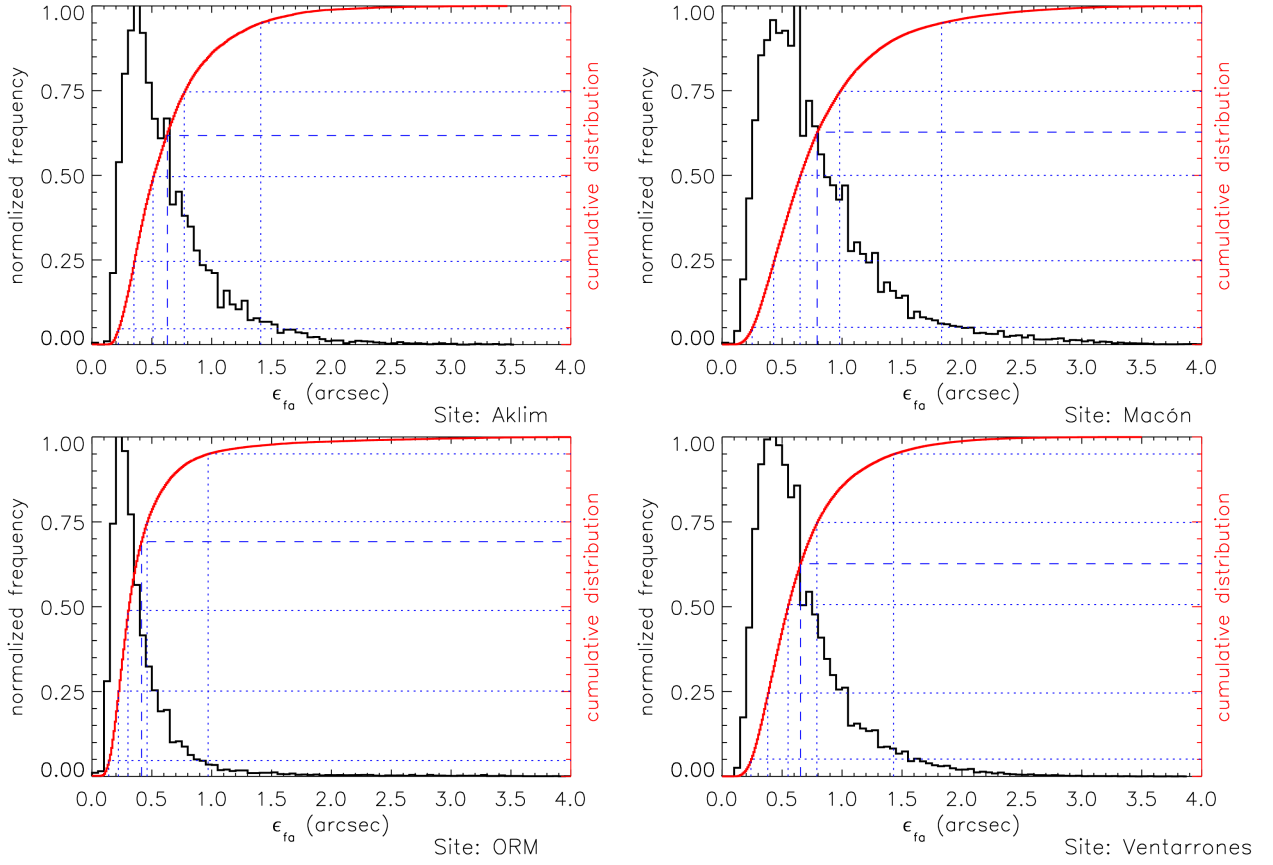


Fig. 6.— Histogram and cumulative distribution of the free atmosphere seeing at each of the four sites.

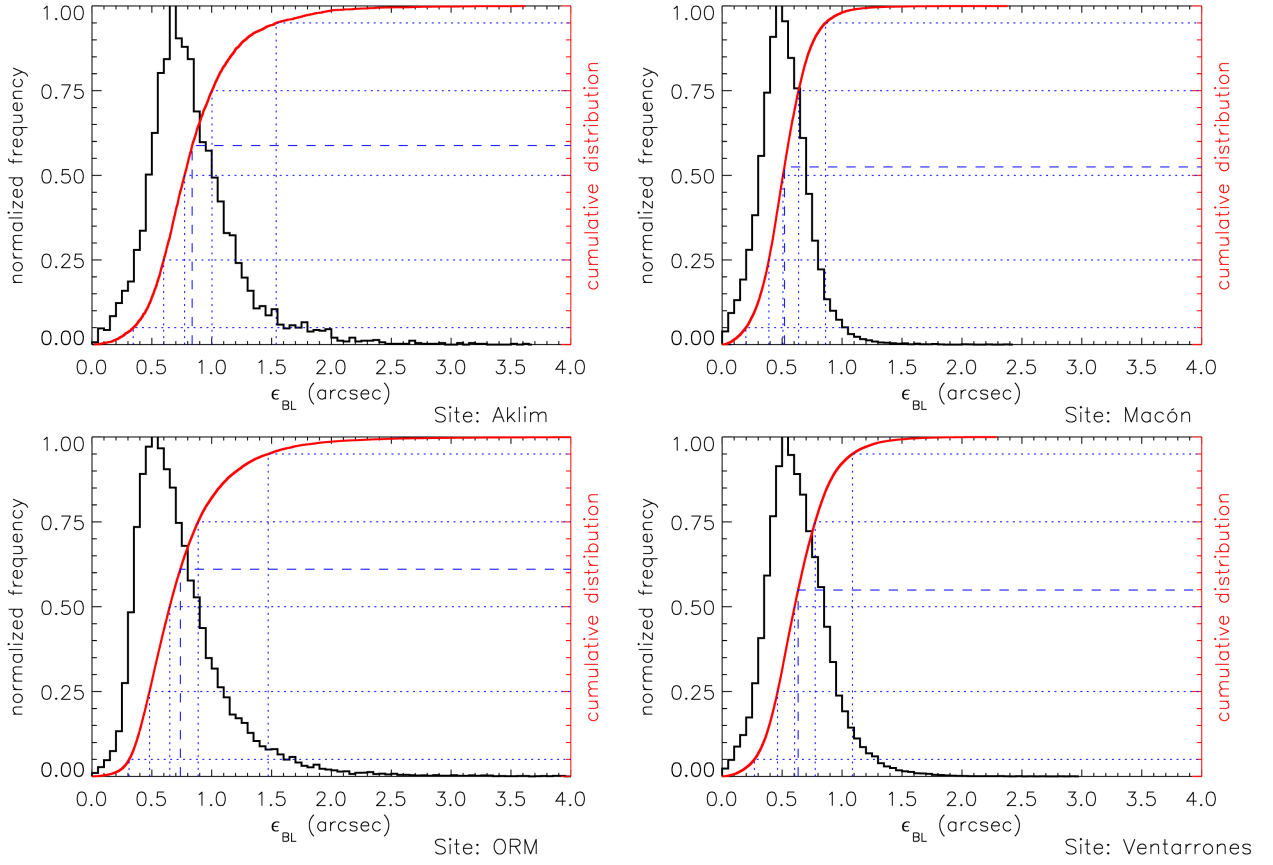


Fig. 7.— Histogram and cumulative distribution of the boundary layer seeing at each of the four sites.

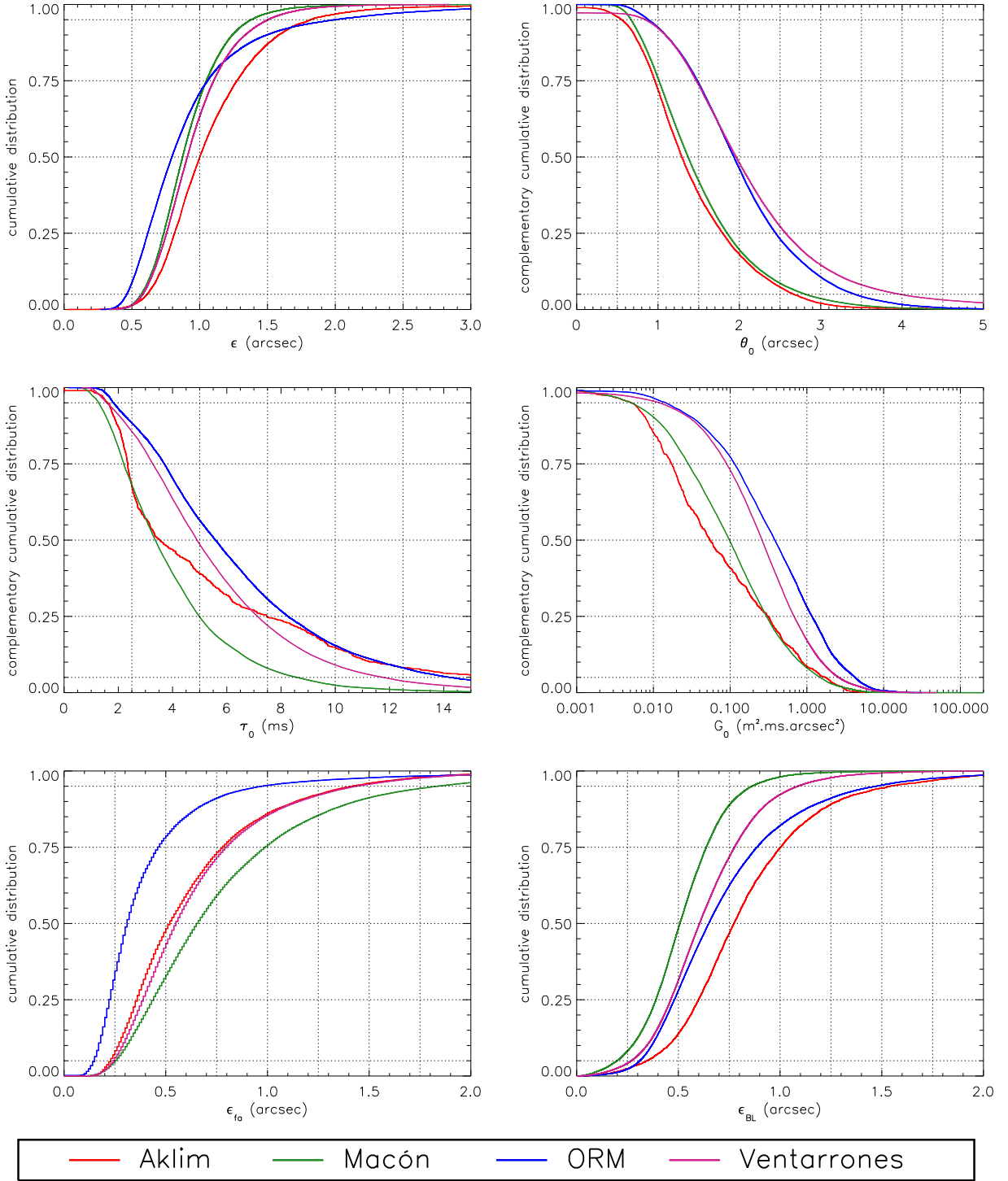


Fig. 8.— From top left to right bottom, cumulative distributions of the integrated seeing, the isoplanatic angle, the coherence time, the ”coherence étendue”, the free atmosphere seeing and the boundary layer seeing of the four candidate sites. In the cases of θ_0 , τ_0 and G_0 the shown curves are the complementary cumulative distributions. Sampling period from April 2008 to May 2009.

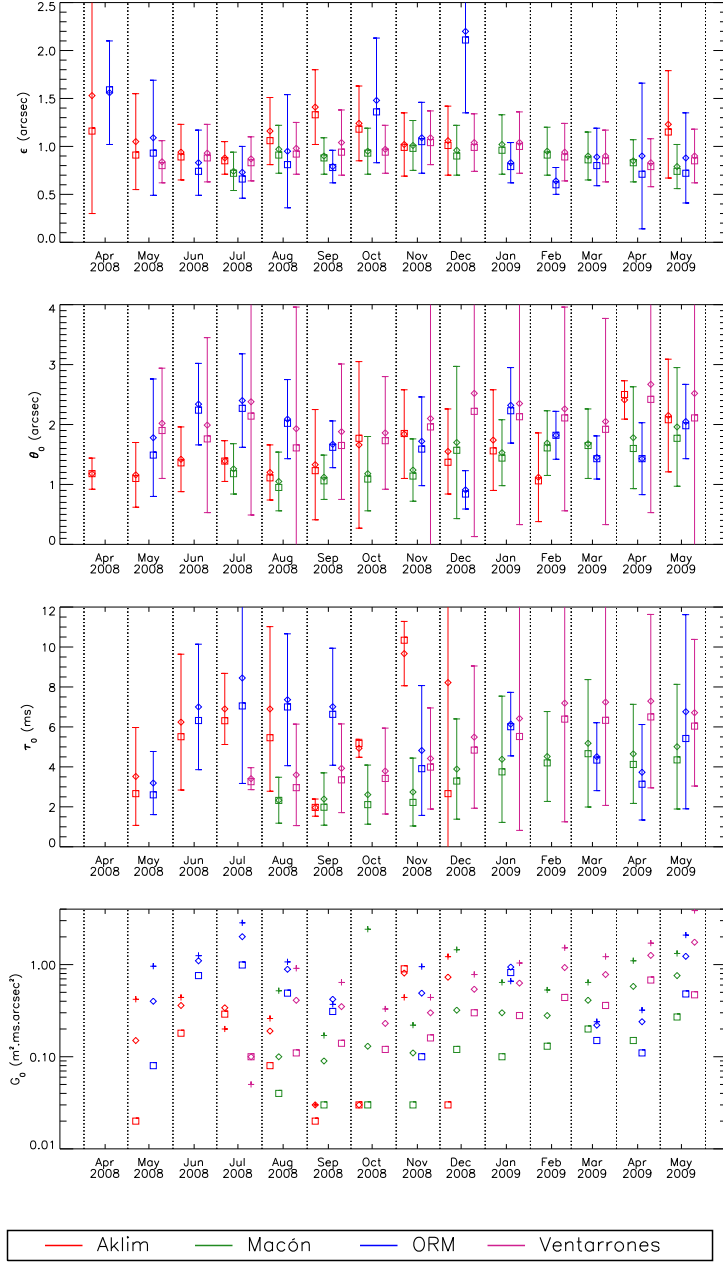


Fig. 9.— Monthly statistics of ϵ , θ_0 , τ_0 , and G_0 at the four candidate sites from April 2008 to May 2009. Mean (diamonds), standard deviation (error bars), and median (squares) values are shown. Points are slightly shifted in time for clarity and months are delimited by vertical dotted lines.

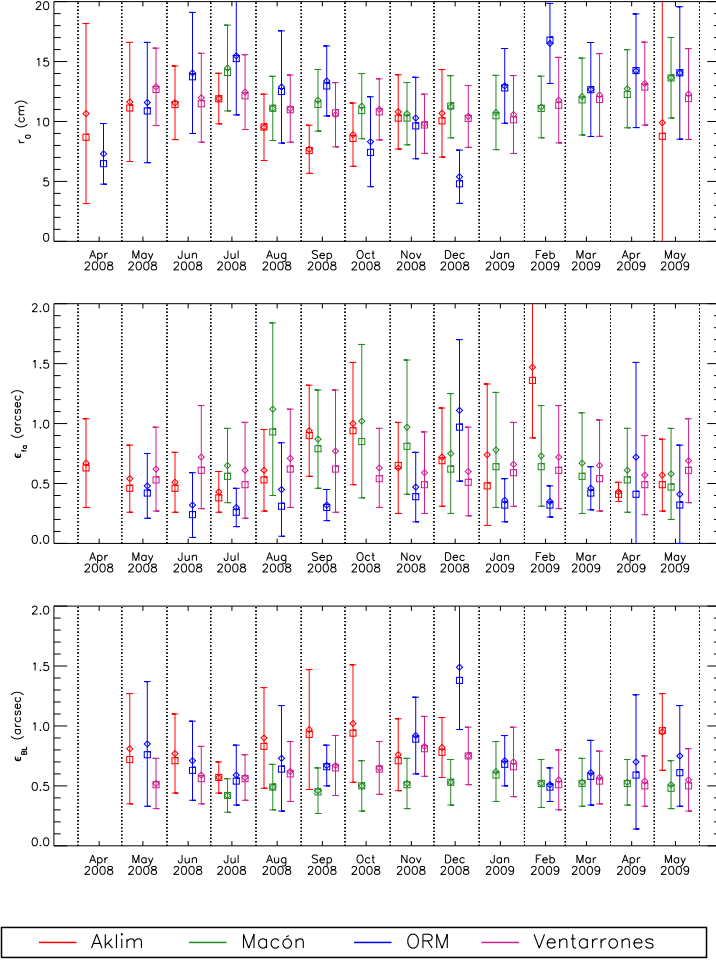


Fig. 10.— Monthly statistics of r_0 , ϵ_{fa} and ϵ_{bl} at the four sites: Aklim, Macón, ORM and Ventarrones during the whole E-ELT site characterization campaign (from April 2008 to May 2009). Mean (diamonds), standard deviation (error bars), and median (squares) values are shown. Points are slightly shifted in time for clarity and months are delimited by vertical dotted lines.

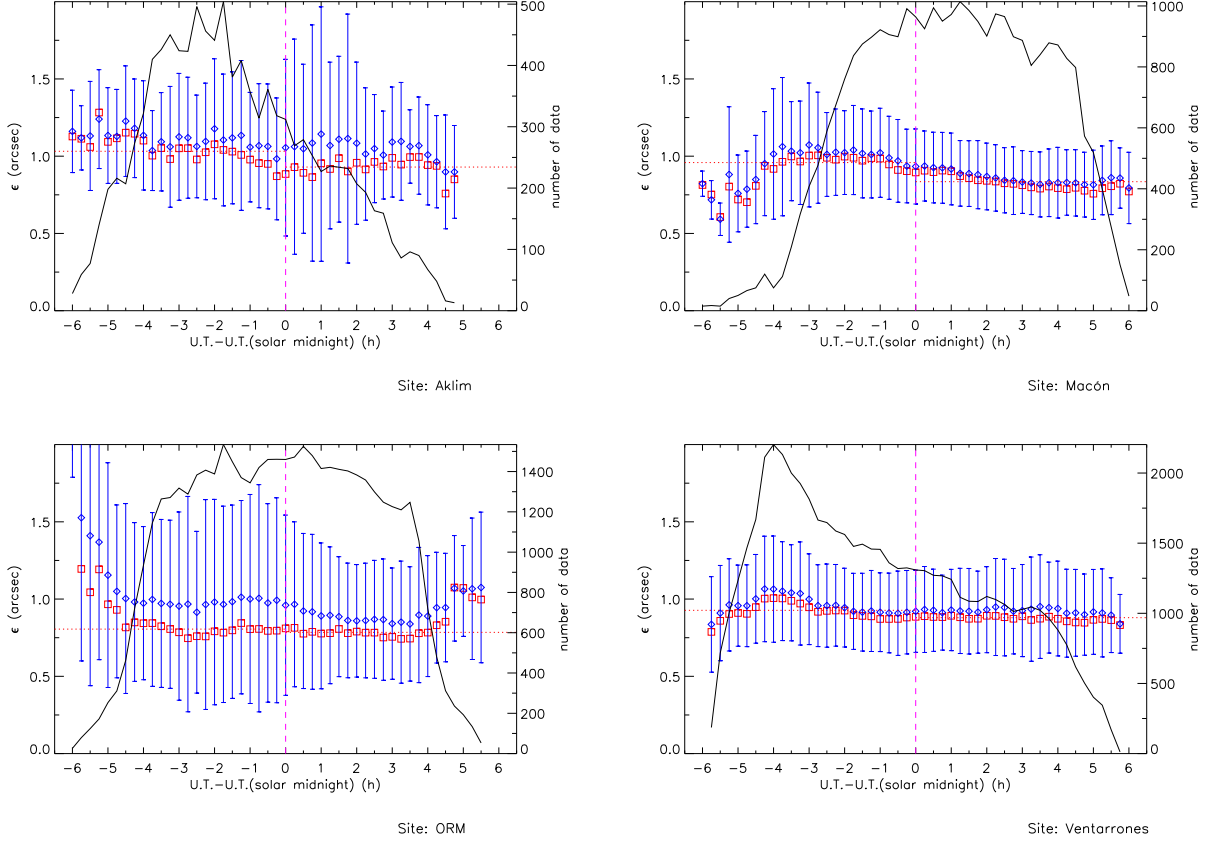


Fig. 11.— Nightly evolution of the seeing deduced from all the nights during the whole observing campaign at the four sites. The median (red squares) and the mean (blue diamonds) of each time interval are shown together with the standard deviation of the mean (error bars) and the number of data (in black).

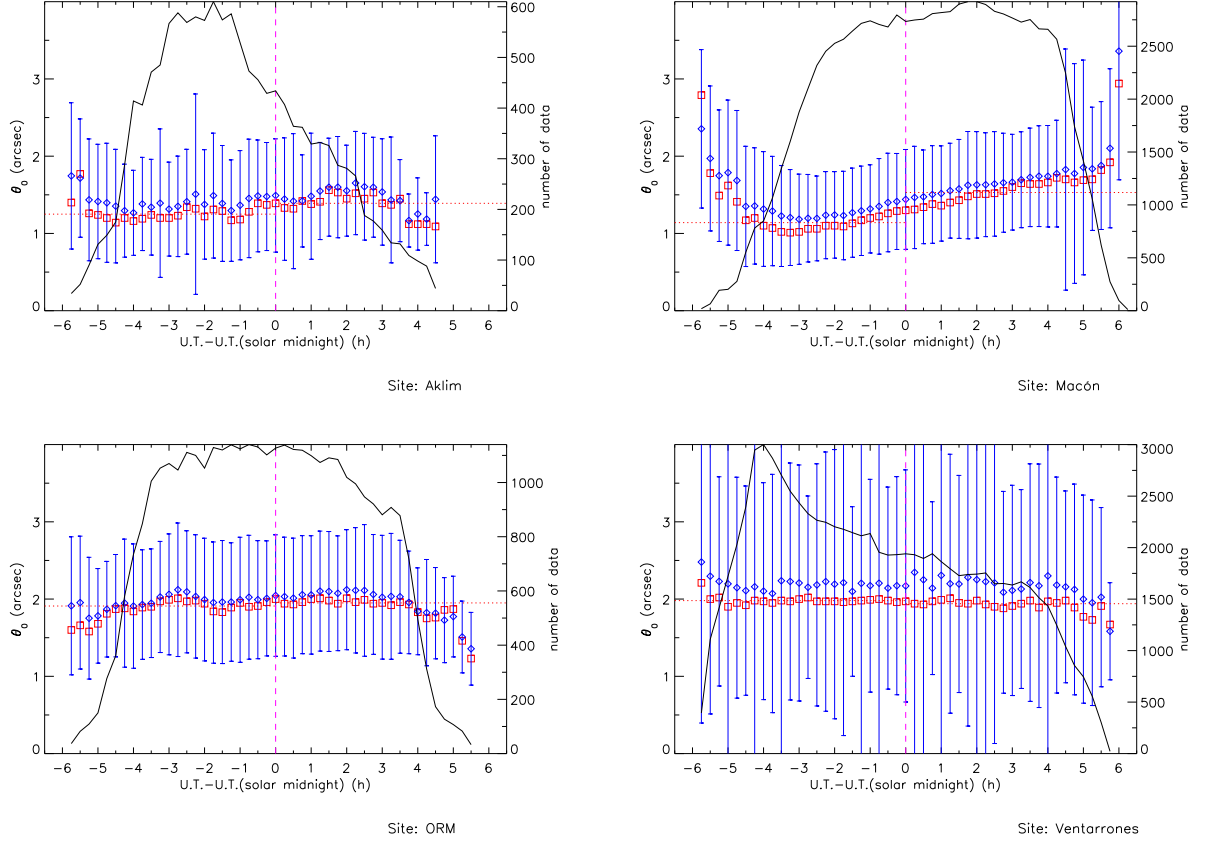


Fig. 12.— Nightly evolution of the isoplanatic angle deduced from all the nights during the whole observing campaign at the four sites. The median (red squares) and the mean (blue diamonds) of each time interval are shown together with the standard deviation of the mean (error bars) and the number of data (in black).

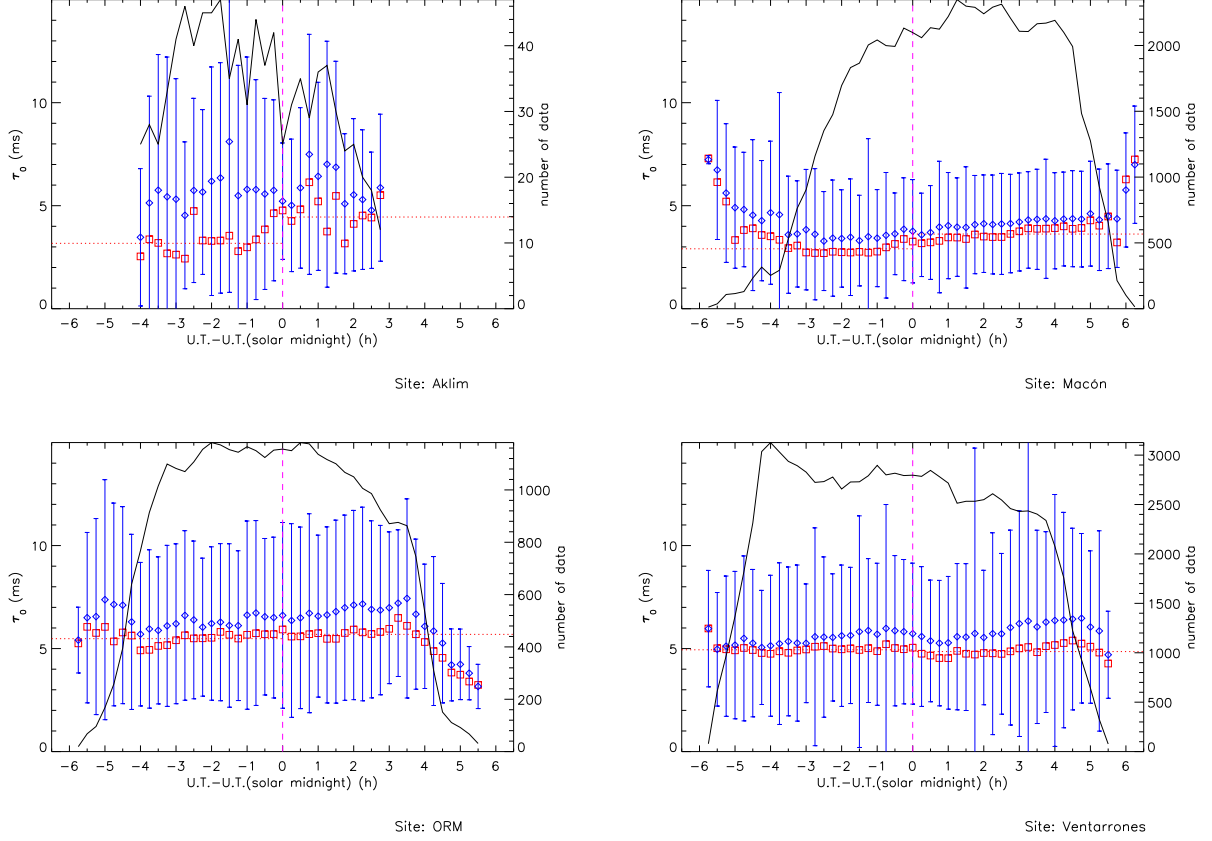


Fig. 13.— Nightly evolution of the coherence time deduced from all the nights during the whole observing campaign at the four sites. The median (red squares) and the mean (blue diamonds) of each time interval are shown together with the standard deviation of the mean (error bars) and the number of data (in black).

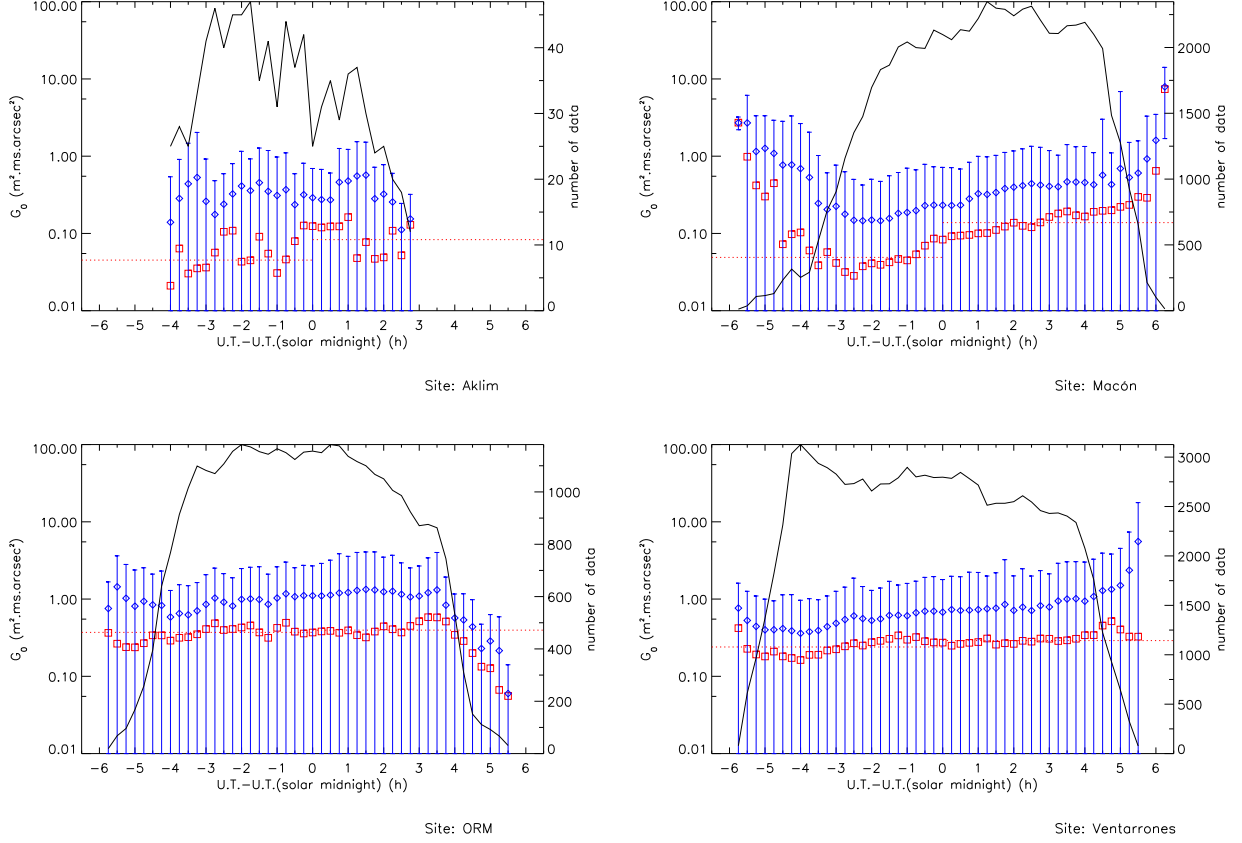


Fig. 14.— Nightly evolution of the coherence étendue deduced from all the nights during the whole observing campaign at the four sites. The median (red squares) and the mean (blue diamonds) of each time interval are shown together with the standard deviation of the mean (error bars) and the number of data (in black).

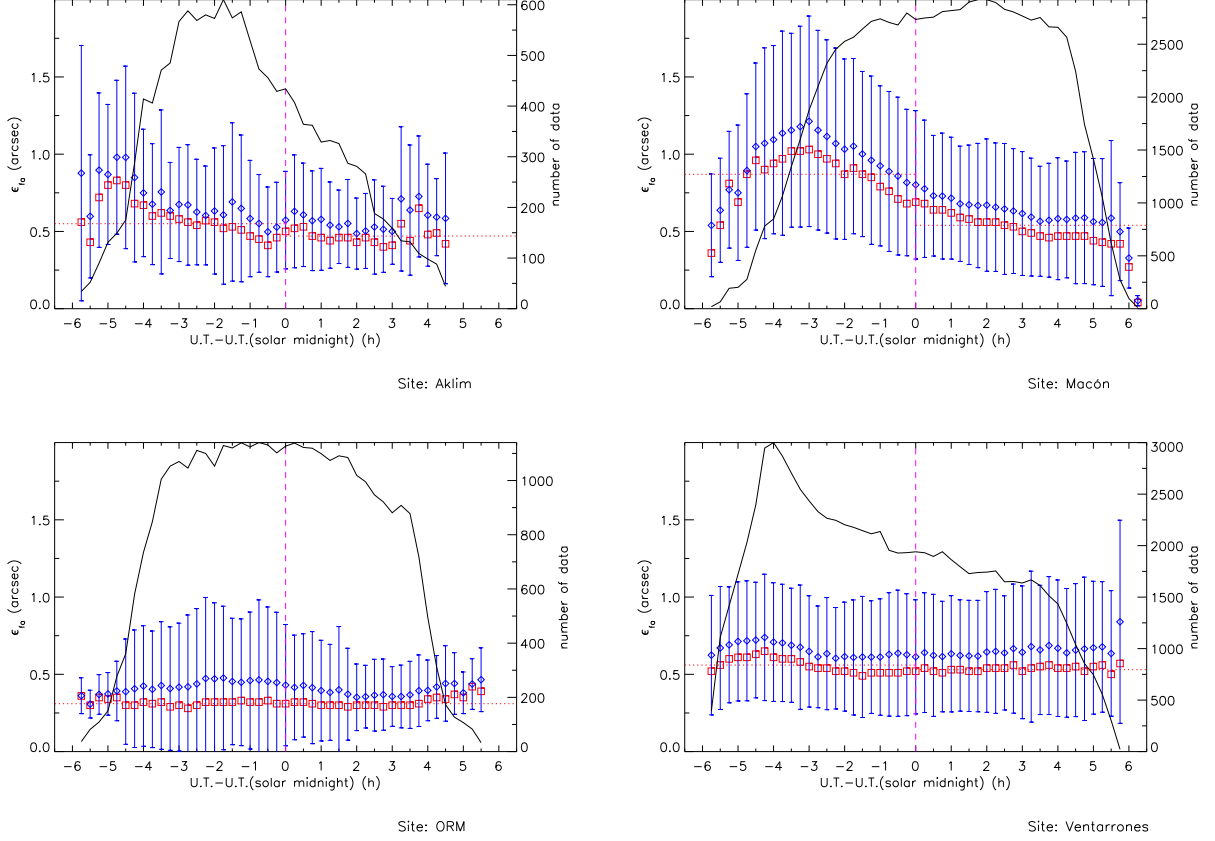


Fig. 15.— Nightly evolution of the free atmosphere seeing deduced from all the nights during the whole observing campaign at the four sites. The median (red squares) and the mean (blue diamonds) of each time interval are shown together with the standard deviation of the mean (error bars) and the number of data (in black).

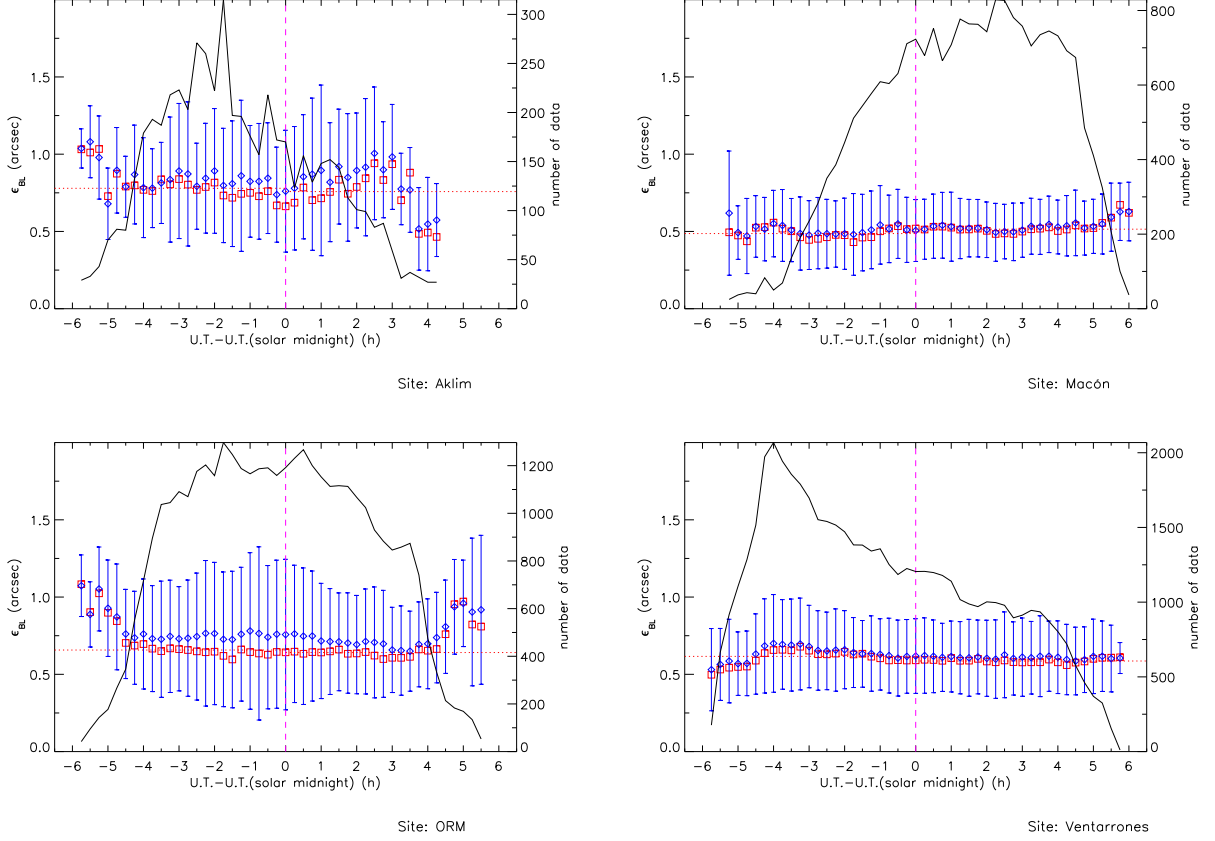


Fig. 16.— Nightly evolution of the boundary layer seeing deduced from all the nights during the whole observing campaign at the four sites. The median (red squares) and the mean (blue diamonds) of each time interval are shown together with the standard deviation of the mean (error bars) and the number of data (in black).

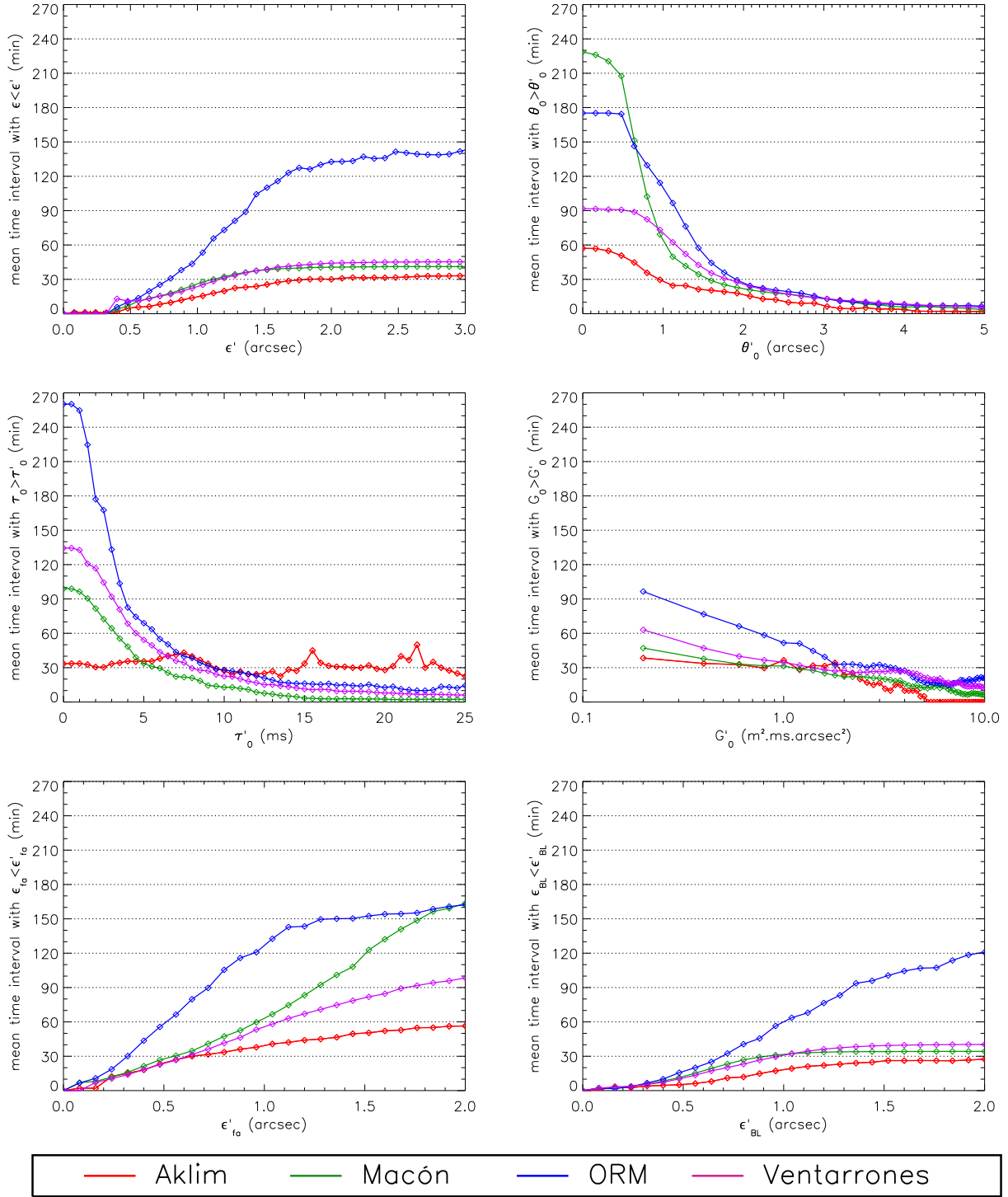


Fig. 17.— Mean time interval during which seeings (total, free and boundary layer) are better (lower) than a given value, and during which isoplanatic angle, coherence time and coherence étendue is better (higher) than a given value.